https://doi.org/10.1016/j.jnoncrysol.2016.06.026

Microstructure and tensile behavior of small scale resistance spot welded sandwich bulk metallic glasses

S.F. Guo[1*, 2], K.C. Chan[3*], Z.Q. Zhu[4], Z.R. Wu[5], W. Chen[6], M. Song[7]

1. Faculty of Materials and Energy, Southwest University, Chongqing 400715, China

2. State Key Laboratory for Mechanical Behavior of Materials, Xi'an Jiaotong University, Xi'an 710049, China

3. Department of Industrial and Systems Engineering, The Hong Kong Polytechnic University, Hong Kong, China

4. School of Mechanical and Electrical Engineering, Nanchang University, Nanchang 330031, China

5. Department of Mechanical Engineering, Iowa State University, Ames, IA 50011, USA

6. Department of Mechanical Engineering and Materials Science, Yale University, New Haven, CT 06511, USA

7. Department of Nuclear Engineering and Radiological Sciences, The University of Michigan, Ann Arbor, MI 48109, USA

Abstract

In this work, a small-scale resistance spot welding method was utilized to join two dissimilar Zr-based bulk metallic glasses and to fabricate the sandwich-laminated metallic glass plates. The laminates exhibit an almost fully amorphous structure without undesirable crystallization. Elemental line scanning across the joint interface shows a uniform distribution of the main elements, demonstrating favorable metallurgical bond in the laminate. The resultant tensile strength of the welded laminate is comparable to that of the parent metallic glasses. The fractured surface of the laminate exhibits extensive multiple failure planes, suggesting that the fracture instability was mediated by a crack branching mechanism over across the joint interface. Such a crack branching mechanism results in a stepwise fracture behavior which is contrastingly different from the conventional single primary shear band dominated catastrophic fracture in monolithic metallic glasses under tension. The unique stepwise fracture behavior endows the sandwiched metallic glass laminates with an excessive strain energy absorption through the joint interface than monolithic metallic glasses. Our results demonstrate that small-scale resistance spot welding is a promising approach to scaling up metallic glasses and to fabricating metallic glass laminates with desirable mechanical performance for structural applications.

Keywords: metallic glasses; tensile behavior; microstructure; laminate

* *E-mail address:* sfguo@swu.edu.cn (S.F. Guo); kc.chan@polyu.edu.hk (K.C. Chan)

1 Introduction

Bulk metallic glasses (BMGs), which offer a range of unique mechanical properties, including high strength, high elasticity, and excellent thermoplastic forming ability, are a newly emerging class of advanced metals [1-4]. Unfortunately, commercialization of these materials for structural or functional applications are so far limited mainly due to two challenges. The first is the limited glass forming ability of BMGs that imposes difficulties in making large scale BMGs. BMGs are metastable alloys that are rapidly frozen from their liquid melts. The required high cooling rate suggests that only small scale specimens can be achieved to attain a glassy structure. For example, even for the relatively robust glass formers such as Zr-based alloys, ~ 1 K/s is required and hence only fully glassy specimens of critical dimension of ~ 10 mm can be achieved. The second challenge is the notorious room temperature plasticity. Whereas BMGs can show limited plasticity under constrained loading modes such as bending or compression, they often exhibit nearly zero plasticity under un-constrained loading modes (e.g., tension), where catastrophic failure behavior of BMGs often acts as a "bottleneck" in their structural applications [5].

Towards the path to the possibility of scaling up BMGs, welding technologies have been effectively employed [6-8]. For example, joining of dissimilar materials such as BMGs and crystalline alloys (Cu, Ti, Al alloys and stainless steel) was successfully developed through a variety of methods, including vaporizing foil actuator [9], friction stir welding [10], explosive welding [11], resistance spot welding [12], and electron beam welding [13]. Joining of similar materials between identical BMG or different BMGs was also investigated by ultrasonic welding [14], laser welding [15], resistance spot welding [16], and friction welding [17]. Among these methods, RSW demonstrates a high potential due to the inexpensive processing cost, high automation, easy operation without filler materials between the weld pieces, as well as high joint quality, especially in sheet materials. These advantages have made RSW one of the most popular processes for assembling parts and components in industrial applications.

More recently, multi-layer metallic glasses were synthesized by magnetron sputtering [18] and thermoplastic bonding [19]. The synthesized laminated metallic glass structures demonstrated an enhanced plasticity under compression or bending conditions. A key question deserving investigation is how the metallic glass laminates behave under un-constrained loading such as tension. In this work, we joined two different Zr-based BMG plates with similar glass transition temperatures by small-scale resistance spot welding (SSRSW) during which a markedly higher cooling rate typically prevails [16]. We systematically

investigated the microstructure, thermal stability, tensile, and fracture behavior of the resulting sandwiched Zr-based BMG laminates. More generally, such BMG laminates offer a novel material model for understanding the deformation behavior of complex or heterogeneous metallic glass structures under un-constrained loading conditions.

2 Experimental

The alloy ingots with nominal composition of $Zr_{62.3}Cu_{22.5}Fe_{4.9}Al_{6.8}Ag_{3.5}$ [20] (labeled as Zr1) and $Zr_{61}Ti_2Cu_{25}Al_{12}$ [21] (labeled as Zr2) were fabricated by arc-melting under a titanium metal gettered argon atmosphere. Sample plates with dimensions of 1.5mm (thickness) × 12mm (width) × 60mm (length) were obtained by copper mold suction-casting method at a vacuum less than 3×10^{-3} Pa. Electrical discharge machining was used to cut 0.4 mm ×12 mm×60 mm sheet specimens from the original BMG plates. The sheet surface was subsequently polished by 2000 grit sandpaper and cleaned with acetone to remove the surface oxide layer and oil stains prior to joining. The welding process was performed on a transistor type micro-resistance spot welding machine MIYACHI MDA-4000B in the air atmosphere. Flat-faced CuCrZr electrodes of 3mm in diameter were used in this study. Fig. 1a shows the welding schematic of the SSRSW for joining the BMG sheets with the order of Zr1/Zr2/Zr1 sandwiched laminates. The SSRSW was carried out with varying welding currents from 1000 to 5000 A using an all-in-one pulsed welding current form. A welding electrode force of 40~70 N and welding time of 3~10 ms were used. Through a systematic study and optimization of the joining parameters, we found that there was no obvious liquid splashing when the welding time was controlled below 3ms, with the welding current below 2500A under a welding force of 50N, as shown in Fig. 1b. As such, three welded samples with about ten welding spots on each sandwiched sheet were successfully fabricated.

The structure of the as-cast and welded samples was identified by X-ray diffraction (XRD, Philips X'Pert PRO) with Cu K_a radiation. The thermal properties were investigated by differential scanning calorimetry (PE, DSC 8000) using ~15 mg samples with Ar as the purge gas at a heating rate of 20 K/min. The microstructure and the elemental distribution along the joint interfaces were determined by a JEOL JSM-6510 scanning electron microscope (SEM) equipped with energy dispersive spectroscopy (EDS). For further observation in the transmission electron microscopy (TEM), the welded region of the sample was prepared into a cross section by focused ion beam (FIB) using a FEI Helios Nanolab 650

Dualbeam FIB with a Ga ion source. A very thin layer of platinum was deposited over the region of interest to avoid excessive Ga ion damage. A 30 kV beam operating at 2.3 nA was used to excavate the sample from both sides of the region to a depth of 5 μm. And then, the sample was thinned further using a final milling beam current of 80 pA. The sample was lifted out in-situ by welding to the micromanipulator and was subsequently moved to a TEM sample holder. Further characterization in a JEOL 3011 was performed for higher magnification and selected area electron diffraction (SAED) analysis. In addition, uniaxial tensile test of the welds was carried out with at least three specimens at room temperature, with a strain rate of 10^{-4} s^{-1} on a MTS 810 material testing system to study the mechanical behavior of welded specimens. The fracture morphologies were also carefully examined using SEM.

3 Results and discussions

Fig. 2 shows the XRD patterns of the as-cast and the welded sandwiched Zr-based BMG panels obtained by collecting and grinding the crushed pieces from the cross-section of the interface into fine powders. The as-cast Zr1 and Zr2 alloys exhibit a broad diffraction halo, suggesting a typical amorphous structure [21, 22]. After the SSRSW, no significant evidence of crystallization was found in the X-ray pattern of the Zr-based BMG laminated interface. This suggests that the welds retain an amorphous nature without devitrification within the detection limit of XRD. Therefore, SSRSW is a well suited method for joining similar BMGs under appropriate welding parameters.

Fig. 3 shows the DSC curves of the as-cast alloys and the welded interface from the joined BMG laminate. Zr1 and Zr2 BMGs both show a distinct glass transition, followed by a wide supercooled liquid region and the crystallization behavior. The two BMGs exhibit a similar glass transition temperature (T_g) of about 648K and 640K, respectively. However, single and two steps of crystallization peaks appear in Zr1 and Zr2 BMGs, respectively below 850 K, which was similarly recorded in previous studies [20, 23]. The crystallization onset temperature T_x and crystallization enthalpy ΔH_{cry} of the two Zr-based BMGs were determined to be approximately 755K and -41.8J/g, 718K and -57.2J/g, respectively. The single-step crystallization implied that the stable crystallization phases were formed during heating the Zr1 alloy above T_g. The two exothermic crystallization peaks of Zr2 alloy may result from the preferential precipitation of some metastable crystalline phases during crystallization. After SSRSW, T_g, T_x and ΔH_{cry} of the interface region from the laminate specimen are 638K, 743K, and -44.2J/g, respectively, displaying similar thermal stabilities to the original alloys. However, the interfaces of the laminate show different

crystallization characteristics from the base alloys, which suggests a slightly different composition of the amorphous phases at the welded interfaces than the original base alloys. Therefore, it is speculated that the SSRSW process may result in gradient amorphous materials [24].

In order to investigate the microstructural evolution and compositional variation at the weld interface, the liquid weld pool (nugget as indicated in Fig. 1a), cross-sectional SEM images, and element line scanning in the vicinity of the joint interface region and heat-affected zone (HAZ) were performed (see Fig. 4a). There are no discernible defects or cracks at the weld interface and HAZ, indicating the formation of a reliable bond between two similar Zr-based BMGs. However, some micro-voids incidentally appear within the base alloys far away from the weld interface. These micro-voids originate from the stacked interface among different layers of BMGs. The sparsely distributed concave weld surfaces may result from the over-loaded welding current level. The EDS elemental line scanning of the joint interface shows a uniform distribution of the main elements, such as Zr, Cu, and Al, in the weld region as shown in Fig. 4b, further demonstrating the formation of metallurgical bond. However, it is challenging to distinguish compositional evolution between Zr1 and Zr2 alloys because of extremely small amounts of total Ag and Fe elements which are beyond the instrument detection capacity. Alternatively, a new amorphous phase with homogenous composition may also form in the weld region and considering that resistance heating is heavily concentrated at the electrode/workpiece interface and the faying interface between workpieces, a faster cooling rate will be expected.

Fig. 5 shows the TEM bright-field images and selected area electron diffraction (SAED) patterns of the weld joint interface prepared by FIB thinning. As indicated in Fig. 5a, it can be clearly observed that there was an interface layer of approximately 500 nm thickness between the two workpieces even if it appears without voids or gaps at the macroscale. Far away from the interface region, fully halo rings without crystalline reflections in the SAEDs of the Zr1 and Zr2 alloys indicate that the alloy consists of only amorphous phase as shown in Fig. 5b. However, a trace amount of crystalline phases is present nearby or within the weld interface for the inner Zr2 BMG due to the relatively poor heat release at the weld interface of dissimilar welds (see Fig. 5c). Along the interface of the Zr2 alloy, the SAED comprises a diffuse amorphous diffraction ring as well as sharp diffraction spots, implying that microscale crystals form in the amorphous matrix (see Fig. 5d). Considering that the FIB thinning was achieved at very low beam current, the crystallization likely originates from the effect of spot welding even at small scale resistance.

These crystalline phases are mainly located along the joint interface during welding process, as confirmed by the dark-field images from the representative two diffraction spots (point 1 and point 2) in the corresponding SAEDs (see Fig. 5e and Fig. 5f, respectively). To further clarify the microstructure of the weld nugget, Fig. 6a-e shows the TEM bright-field images and SAEDs of the central region of the joint interface corresponding the regions labeled as A, B and C in Fig. 5a, respectively. It can be seen that the central region of the joint interfaces is mainly amorphous with a small amount of crystalline phases. Note that diffraction from crystals causes several overlapping spot patterns, making it difficult to index (Fig. 6b and f). In addition, it should be noted that the corresponding SAED pattern from region B is identified to be hexagonal close packed (hcp) Zr solid solution phases (Fig. 6d), which is different from the previous report that stable $CuZr_2$ phase preferentially precipitates in as-cast ZrCu-based BMGs [20]. This may result from the strong thermo-mechanical coupling during the process of micro-resistance spot welding. Furthermore, the welding parameters such as weld time, weld current, and the electrode force of the present work are systematically lower than the previous work used in Ti-based BMGs by RSW [25]. Similarly, the metallic glass ribbons of Vitreloy 101 with minor crystallization can be prepared by SSRSW in previous study [26]. These features suggest that the SSRSW technology is an ideal candidate for applications in the field of small-scale BMGs, especially in the micro electro-mechanical system devices whereby microstructure stability is required to avoid over-crystallization [27].

Samples for the uniaxial tensile test were fabricated with a gauge length of 6 mm and gauge width of 1.5 mm by wire-cutting from the welds, as shown in the inset of Fig. 7. The two parent Zr-based BMGs, although showing large compressive plasticity and high fracture toughness, exhibit almost zero tensile ductility [21, 28]. There is no obvious difference in mechanical behavior of Zr1 and Zr2 alloys under tension. In the present work, the stress strain curve of Zr1 alloy is shown as an example. Macroscopically, the BMG sandwiched laminates display an overall elastic behavior without macroscopic plastic yielding, which is similar to the typical tensile characteristics of monolithic BMGs. However, interestingly, the sandwiched laminates fail in a stepwise manner associated with a “serrated” fracture arising from the delamination process during crack propagation. Specifically, at a stress level of ~ 1200 MPa in the tensile stress–strain curve, the stress suddenly drops to ~ 900 MPa, and subsequently recovers to ~ 1200 MPa prior to the ultimate catastrophic failure (see Fig. 7). The initial fracture strength of the sandwiched laminate is subtly lower than that of the parent monolithic BMGs, and can be rationalized by the stress concentration

effect at the joint interfaces. In general, the joined interface with a thickness of ~ 500 nm is imperfect (Fig. 5a). If we assume each interface contains a number of "micro-cracks" (welding defects such as micro-voids), the laminate can be regarded as a monolithic bulk material containing several arrays of "micro-cracks". The fracture strength of the laminate can hence be correlated with the Mode I initiation fracture toughness [8, 29], K_I, of the laminate by $K_I = \sigma\sqrt{\pi a} f(\frac{a}{W})$. Thus, $\sigma = \frac{K_I}{\sqrt{\pi a} f(\frac{a}{W})}$, where a and W are the micro-crack length and spacing, respectively. $f(\frac{a}{W})$ denotes a complex geometric correction factor function, which is typically a finite value, and is related to the crack geometry and the material itself. This classical linear elastic fracture mechanics model essentially illustrates a stress concentration effect brought by the micro-cracks. As such, it is understandable that the initial fracture stress of the laminate is lower than the monolithic parent materials. However, it is of interest that the sandwiched laminate structure apparently shows an increased resistance to crack growth. The stress-strain curve shows a “serrated” behavior and the laminate proceeds to carry load and undergo plastic deformation even after the initial fracture event. Microscopically, this limited plastic deformation stems from the crack branching and delamination across the joint interface (see Fig. 8 below), which contribute to an enhanced fracture energy absorption prior to the ultimate fracture instability. This is further corroborated by ~ 8% increase of the area under the stress-strain curves. Such crack branching and delamination mechanism results in the unique stepwise fracture mode which is contrastingly different from the conventional purely elastic catastrophic failure mode for monolithic metallic glasses under tension [30]. The stepwise fracture behavior promotes a protective fracture mechanism and facilitates a higher energy absorption capability. Practically, the introduced tensile behavior of the metallic glass laminate provides a novel insight into developing tougher BMGs, especially under un-constrained loading.

Fig. 8 shows the SEM images of the fractured morphologies of the sandwiched laminate. Tensile fracture occurs along the maximum resolved shear stress orientation inclined along ~ 45° to the loading axis (see Fig. 8a). Although the shear fracture mode is manifested in the laminate, there are few shear bands in the vicinity of the shear fractured plane. However, the corresponding fracture surface is unambiguously not planar (see Fig. 8b), implying that the shear deformation and crack instability are not carried out through one single dominant shear band. On the other hand, the extensive multiple failure planes found on

the fractured surface suggest a crack deflection mechanism during the delamination process under loading, which is also reflected by the crack bifurcation or branching on the side surface (see Fig. 8a). On the fractured surface, several clear shear offsets are present at the edge of each individual constitutional plates in the laminate (see Fig. 8c and d). The multiple shear offsets originate from the delamination mediated stepwise fracture behavior and are distinct from the typical single shear offset on the fractured surface of a monolithic metallic glass [31]. The crack branching behavior and the multiple shear offsets result in an enhanced energy absorption through the joint interface which deflects the crack propagation and thus suppresses the otherwise catastrophic instability in monolithic metallic glasses. Therefore, higher crack resistance and higher fracture toughness (the area under the stress-strain curve) are achieved in the laminate than in the monolithic metallic glasses. In the interior of each laminated layer, plentiful patterns such as radiative cores with some liquid features and "river-like" patterns reveal shear induced local melting during the fracture process [31]. The coexistence of these multiple surface morphologies demonstrates the key role that the interface plays in affecting the mechanical behavior of the welded laminate.

4 Conclusions

$Zr_{62.3}Cu_{22.5}Fe_{4.9}Al_{6.8}Ag_{3.5}$ and $Zr_{61}Ti_2Cu_{25}Al_{12}$ BMGs sandwich-laminated plates are successfully prepared by small-scale resistance spot welding. A satisfactory metallurgical bond is achieved in the welded region, where a uniform distribution of the main elements without elemental mutation is revealed. Transmission electron microscopy at the welding interface demonstrates an almost amorphous feature. The resultant sandwiched laminate shows a stepwise fracture behavior, which can be attributed to a unique crack branching mechanism. The fractured surface of the laminate exhibits extensive multiple failure planes, implying that the crack propagation is collectively associated with a crack branching mechanism across the welding interface. Our findings demonstrate that small-scale resistance spot welding technology is a promising candidate for scaling up metallic glasses and for fabricating heterogeneous metallic glass laminates with desirable properties for structure applications.

Acknowledgements

This work was financially supported by the Research Grants Council of the Hong Kong Special Administration Region (No. PolyU511108), National Natural Science Foundation of China (No. 51301142),

Chongqing Research Program of Basic Research and Frontier Technology (No. cstc2015jcyjBX0107), the Fundamental Research Funds for the Central Universities (No. XDJK2014B027), and the Open Project Program of State Key Laboratory for Mechanical Behavior of Materials, Xi'an Jiaotong University (No. 20121202).

References

[1] W.L. Johnson, Bulk Glass-Forming Metallic Alloys: Science and Technology, MRS Bull 24 (1999) 42-56.

[2] W.H. Wang, C. Dong, C.H. Shek, Bulk metallic glasses, Mater. Sci. Eng. R. 44 (2004) 45-89.

[3] J. Schroers, Processing of Bulk Metallic Glass, Adv. Mater. 22 (2010) 1566-1597.

[4] S.F. Guo, J.L. Qiu, P. Yu, S.H. Xie, W. Chen, Fe-based bulk metallic glasses: Brittle or ductile?, Appl. Phys. Lett. 105 (2014) 161901.

[5] C.A. Schuh, T.C. Hufnagel, U. Ramamurty, Mechanical behavior of amorphous alloys, Acta Mater. 55 (2007) 4067-4109.

[6] A.J. Swiston Jr., T.C. Hufnagel, T.P. Weihs, Joining bulk metallic glass using reactive multilayer foils, Scripta Mater. 48 (2003) 1575-1580.

[7] Y. Kawamura, Liquid phase and supercooled liquid phase welding of bulk metallic glasses, Mater. Sci. Eng. A 375-377 (2004) 112-119.

[8] W. Chen, Z. Liu, J. Schroers, Joining of bulk metallic glasses in air, Acta Mater. 62 (2014) 49-57.

[9] A. Vivek, M. Presley, K.M. Flores, N.H. Hutchinson, G.S. Daehn, Solid state impact welding of BMG and copper by vaporizing foil actuator welding, Mater. Sci. Eng. A 634 (2015) 14-19.

[10] H.S. Shin, Tool geometry effect on the characteristics of dissimilar friction stir spot welded bulk metallic glass to lightweight alloys, J. Alloys Comp. 586 (2014) S50-S55.

[11] M.Q. Jiang, B.M. Huang, Z.J. Jiang, C. Lu, L.H. Dai, Joining of bulk metallic glass to brass by thick-walled cylinder explosion, Scripta Mater. 97 (2015) 17-20.

[12] Y.F. Sun, H. Fujii, Microstructure and mechanical properties of dissimilar spot friction stir welded $Zr_{55}Cu_{30}Al_{10}Ni_5$ bulk metallic glass to pure copper, Intermetallics 33 (2013) 113-119.

[13] S. Kagao, Y. Kawamura, Y. Ohno, Electron-beam welding of Zr-based bulk metallic glasses, Mater. Sci. Eng. A 375–377 (2004) 312-316.

[14] J.G. Wang, J.C. Fan, Y.F. Zhang, G. Wang, W.H. Wang, K.C. Chan, Diffusion bonding of a Zr-based

metallic glass in its supercooled liquid region, Intermetallics 46 (2014) 236-242.

[15] G. Wang, Y.J. Huang, M. Shagiev, J. Shen, Laser welding of $Ti_{40}Zr_{25}Ni_3Cu_{12}Be_{20}$ bulk metallic glass, Mater. Sci. Eng. A 541 (2012) 33-37.

[16] K. Fujiwara, S. Fukumoto, Y. Yokoyama, M. Nishijima, A. Yamamoto, Weldability of $Zr_{50}Cu_{30}Al_{10}Ni_{10}$ bulk glassy alloy by small-scale resistance spot welding, Mater. Sci. Eng. A 498 (2008) 302-307.

[17] C.H. Wong, C.H. Shek, Friction welding of $Zr_{41}Ti_{14}Cu_{12.5}Ni_{10}Be_{22.5}$ bulk metallic glass, Scripta Mater. 49 (2003) 393-397.

[18] S.Y. Kuan, H.S. Chou, M.C. Liu, X.H. Du, J.C. Huang, Micromechanical response for the amorphous/amorphous nanolaminates, Intermetallics 18 (2010) 2453-2457.

[19] J. Ma, K.C. Chan, L. Xia, S.H. Chen, F.F. Wu, W.H. Li, W.H. Wang, Multi-layer laminated Pd-based metallic glass with enhanced plasticity, Mater. Sci. Eng. A 587 (2013) 240-243.

[20] S.F. Guo, H.J. Zhang, Z. Liu, W. Chen, S.F. Xie, Corrosion resistances of amorphous and crystalline Zr-based alloys in simulated seawater, Electrochem. Commun. 24 (2012) 39-42.

[21] Q. He, Y.Q Cheng, E. Ma, J. Xu, Locating bulk metallic glasses with high fracture toughness Chemical effects and composition optimization, Acta Mater. 59 (2011) 202-215.

[22] S.F. Guo, Z. Liu, K.C. Chan, W. Chen, H.J. Zhang, J.F. Wang, P. Yu, A plastic Ni-free Zr-based bulk metallic glass with high specific strength and good corrosion properties in simulated body fluid, Mater. Lett. 84 (2012) 81-84.

[23] Q. He, J. Xu, Locating Malleable Bulk Metallic Glasses in Zr–Ti–Cu–Al Alloys with Calorimetric Glass Transition Temperature as an Indicator, J. Mater. Sci. Technol. 28 (2012) 1109-1122.

[24] K.G. Vishnu, M.J. Cherukara, H. Kim, A. Strachan, Amorphous Ni/Al nanoscale laminates as high-energy intermolecular reactive composites, Phys. Rev. B 85 (2012) 184206.

[25] D. Makhanlall, G. Wang, Y.J. Huang, D.F. Liu, J. Shen, Joining of Ti-based bulk metallic glasses using resistance spot welding technology, J. Mater. Process. Technol. 212 (2012) 1790-1795.

[26] N. Baca, T.T. Ngo, R.D. Conner, S.J. Garrett, Small Scale Resistance Spot Welding of $Cu_{47}Ti_{34}Zr_{11}Ni_8$ (Vitreloy 101) Bulk Metallic Glass, J. Mater. Process. Technol. 213 (2013) 2042-2048.

[27] J. Ketkaew, Z. Liu, W. Chen, Jan Schroers, Critical Crystallization for Embrittlement in Metallic

Glasses, Phys. Rev. Lett. 115 (2015) 265502.

[28] Y. Liu, Y.M. Wang, H.F. Pang, Q. Zhao, L. Liu, A Ni-free ZrCuFeAlAg bulk metallic glass with potential for biomedical applications, Acta Biomater. 9 (2013) 7043-7053.

[29] H. Tada, P.C. Paris, G.R. Irwin, The Stress Analysis of Cracks Handbook, third edition, American Society of Mechanical Engineers, New York, 2000.

[30] Y. Leng, T.H. Courtney, Some tensile properties of metal-metallic glass laminates, J. Mater. Sci. 24 (1989) 2006-2010.

[31] B.A. Sun, W.H. Wang, The fracture of bulk metallic glasses, Prog. Mater. Sci. 74 (2015) 211-307.

Figure captions

Fig. 1 Schematic illustration of small-scale resistance spot welding of BMG sandwiched laminates (a) and the optimized welding parameters (b).

Fig. 2 XRD patterns of the as-cast and welding laminated Zr-based BMGs.

Fig. 3 The DSC curves of the parental and laminated BMGs at a heat rate of 20K/min.

Fig. 4 Cross-sectional SEM images and EDS elemental line scanning in the interfacial region of the laminate.

Fig. 5 The bright-field TEM images of the joint interface (a) and the Zr2 alloy (c); the corresponding SAED patterns (b, d) and dark-filed TEM images (e, f).

Fig. 6 The bright-field TEM images of regions labeled A, B and C in Fig. 5(a) and the corresponding SAED patterns.

Fig. 7 Uniaxial tensile stress–strain curves of the sandwiched laminate and the morphology of the undeformed specimen shown in inset.

Fig. 8 SEM images of the fractured morphologies of the sandwiched laminate.

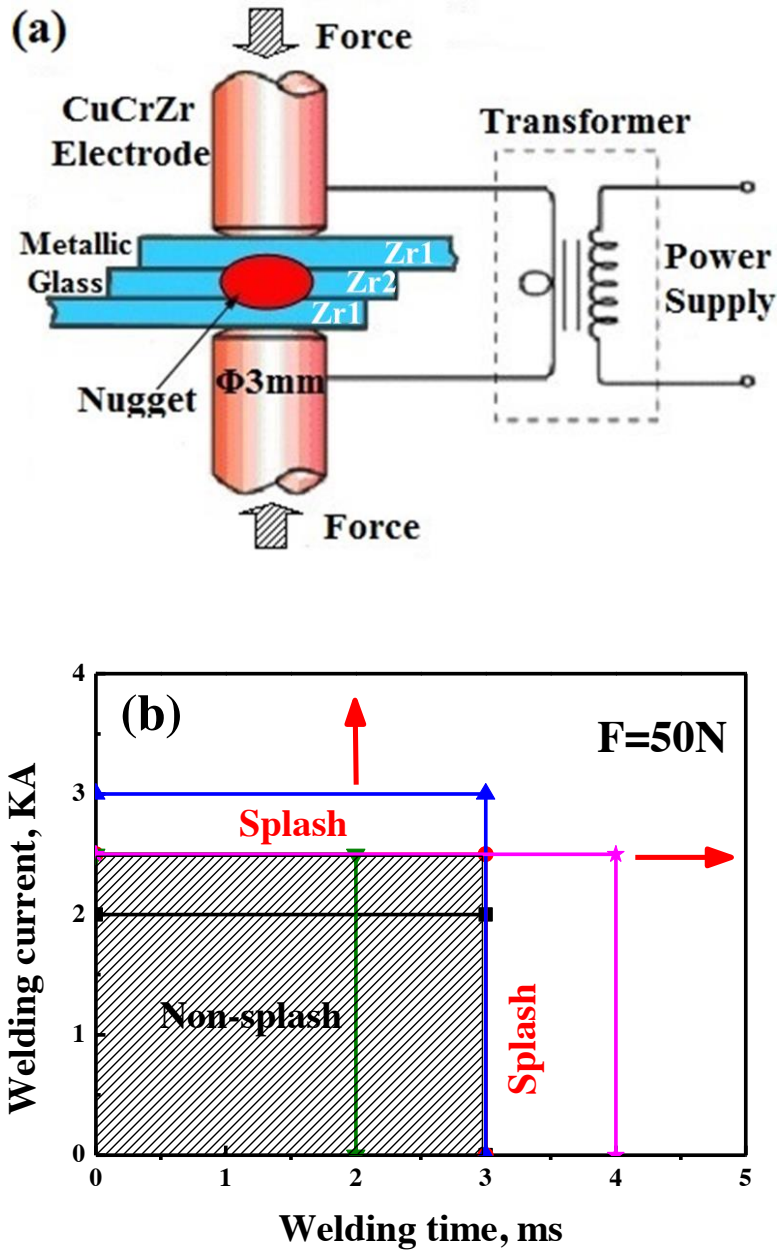
(a)
Force
CuCrZr
Electrode
Transformer
Metallic
Glass
Zr1
Zr2
Zr1
Power
Supply
Nugget
Φ3mm
Force
(b)
F=50N
Splash
Non-splash
Splash
Welding current, KA
Welding time, ms
0
1
2
3
4
5

Fig. 1

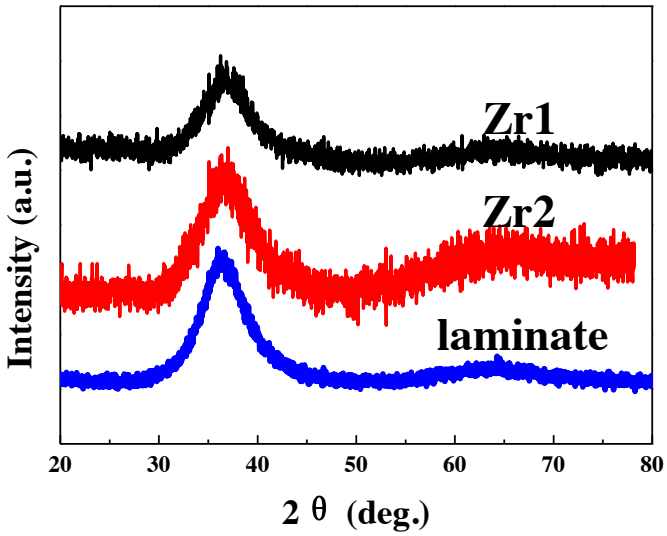

Fig. 2

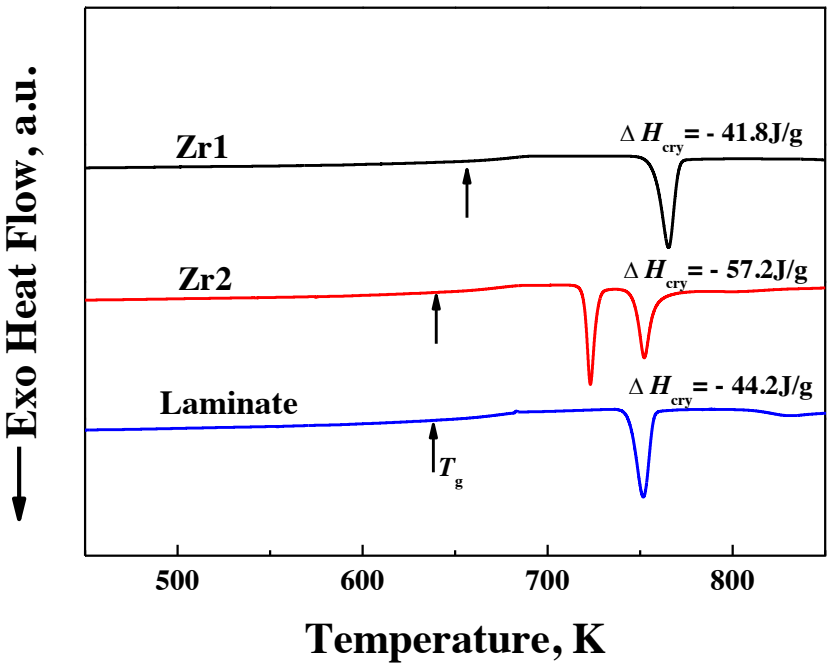
Exo Heat Flow, a.u.
Zr1
Δ H cry = - 41.8J/g
Zr2
Δ H cry = - 57.2J/g
Laminate
Δ H cry = - 44.2J/g
T g
500
600
700
800
Temperature, K

Fig. 3

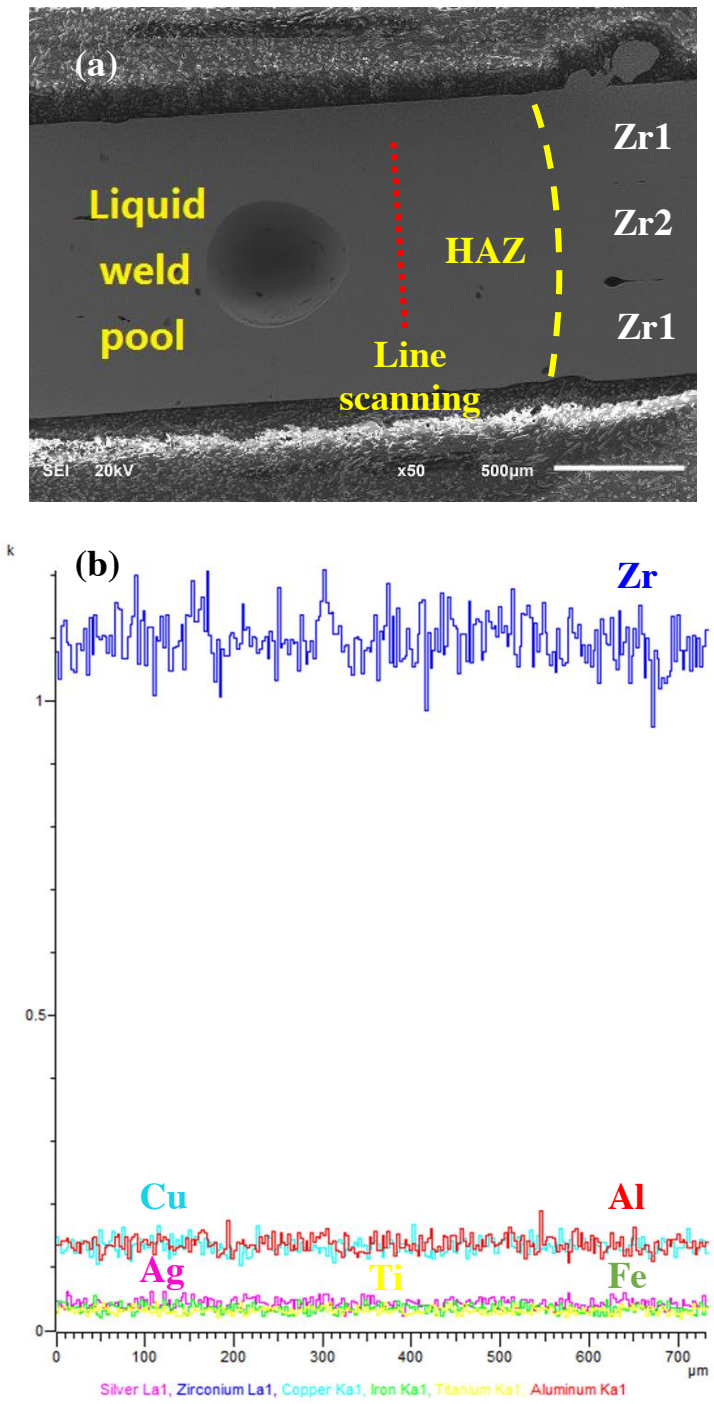
(a)
Liquid
weld
pool
HAZ
Line
scanning
Zr1
Zr2
Zr1
SEI 20kV
x50
500μm
(b)
Zr
Cu
Al
Ag
Ti
Fe
k
1
0.5
0
0
100
200
300
400
500
600
700
μm
Silver La1, Zirconium La1, Copper Ka1, Iron Ka1, Titanium Ka1, Aluminum Ka1

Fig. 4

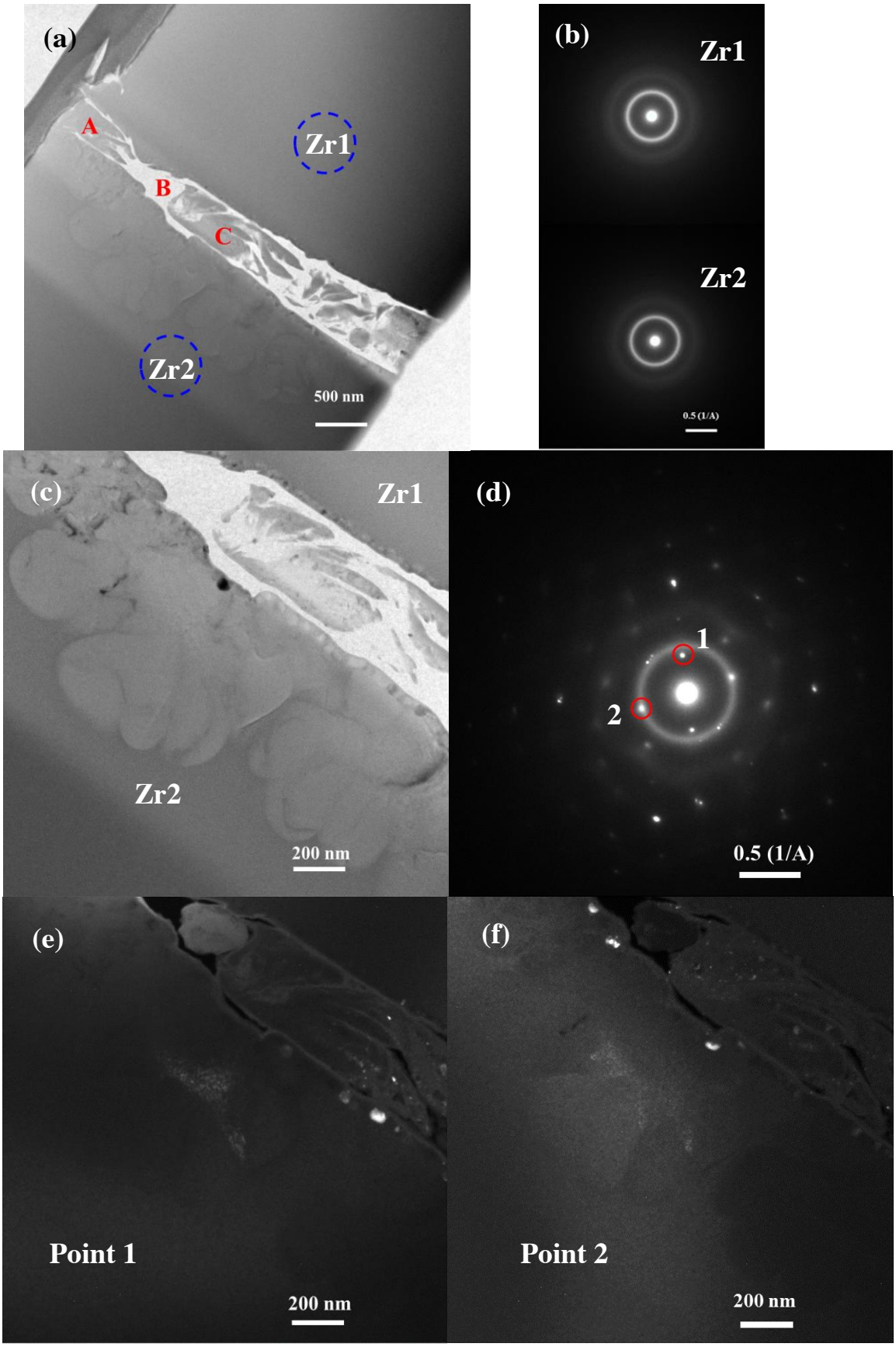
(a)
A
B
C
Zr1
Zr2
500 nm
(b)
Zr1
Zr2
0.5 (1/A)
(c)
Zr1
Zr2
200 nm
(d)
1
2
0.5 (1/A)
(e)
Point 1
200 nm
(f)
Point 2
200 nm

Fig. 5

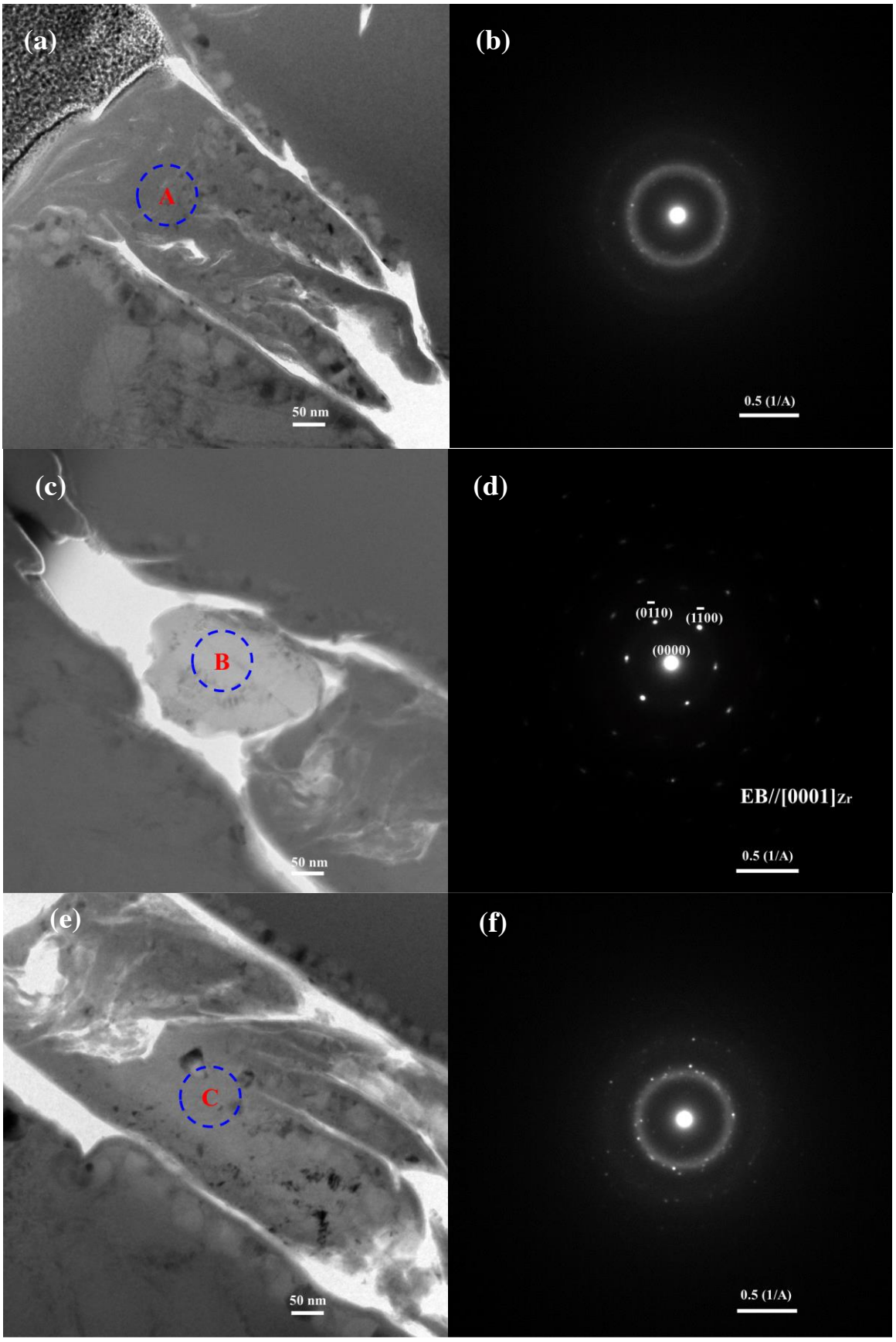
(a)
A
50 nm
(b)
0.5 (1/A)
(c)
B
50 nm
(d)
(0$\bar{1}$10)
(1$\bar{1}$00)
(0000)
EB//[0001]Zr
0.5 (1/A)
(e)
C
50 nm
(f)
0.5 (1/A)

Fig. 6

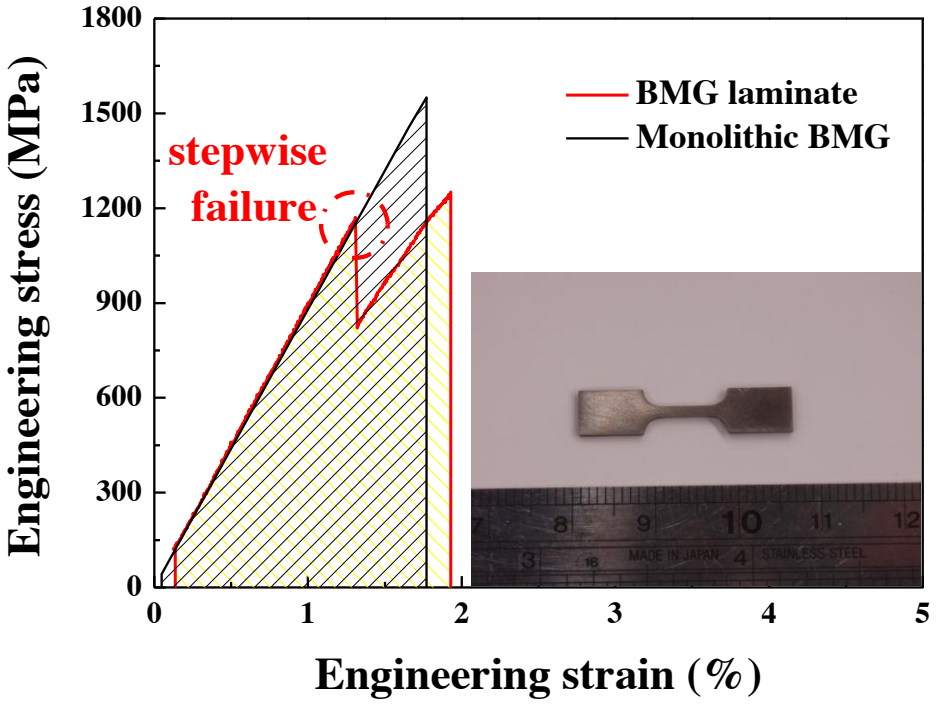
Engineering stress (MPa)
1800
1500
1200
900
600
300
0
0
1
2
3
4
5
Engineering strain (%)
stepwise
failure
BMG laminate
Monolithic BMG

Fig. 7

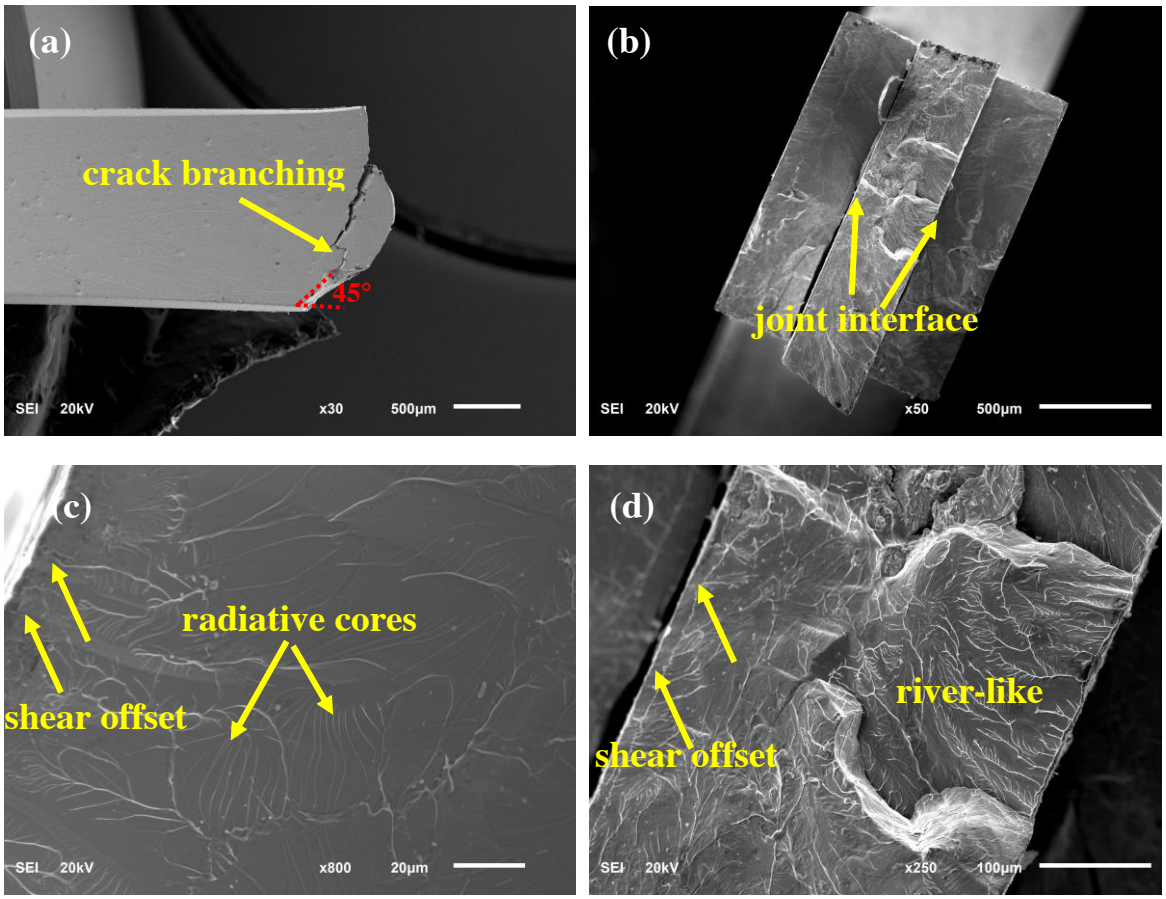
(a)
crack branching
45°
SEI 20kV x30 500μm
(b)
joint interface
SEI 20kV x50 500μm
(c)
radiative cores
shear offset
SEI 20kV x800 20μm
(d)
river-like
shear offset
SEI 20kV x250 100μm

Fig. 8